Supporting Information

Sub-5 nm ZnCoS shell on Co core via chemical vapor reconstruction: ultra-thin heterointerface enabling efficient oxygen electrocatalysis in zinc-air batteries

Xiangjun Zheng[a,#], *Wenhua Shi*[a,#], *Yaman Cui*[a], *Jiayu Zhao*[a], *Qianqian Fan*[a], *Zhongyao Duan*[a], *Yuanjun Liu*[a], *Xingmei Guo*[a], *Junhao Zhang*[a,*], *Ruizhi Yang*[b,*]

Address

[a] School of Environmental and Chemical Engineering, Jiangsu University of Science and Technology, Zhenjiang 212003, China

[b] College of Energy, Soochow Institute for Energy and Materials InnovationS, Soochow University, Suzhou 215006, P. R. China

*Corresponding author

E-mail: jhzhang6@just.edu.cn (J. Zhang); yangrz@suda.edu.cn (R. Yang).

[#]These authors contribute equally to this work.

EXPERIMENTS

1.1. Chemicals.

Thiourea (CH_4N_2S), cobaltous nitrate hexahydrate ($Co(NO_3)_2{\cdot}6H_2O$), 2-Methylimidazole (2-MIM, $C_4H_6N_2$), platinum carbon (Pt/C, 20 wt%), ruthenium dioxide (RuO_2) and potassium hydroxide (KOH, 95%) were purchased from Aladdin Reagent Co. Ltd. Zinc nitrate hexahydrate ($Zn(NO_3)_2{\cdot}6H_2O$), ethylene glycol ($(CH_2OH)_2$), ethanol (C_2H_5OH), acetone (CH_4O), zinc acetate ($Zn(CH_3COO)_2$) and polyvinyl pyrrolidone (PVP, $(C_6H_9NO)_n$) were obtained from Sinopharm Chemical Reagent Co., Ltd (China). Nafion solution (5 wt%, D520) was sourced from DuPont Co., Ltd.

1.2. Synthesis of catalysts.

ZnS NPs: A precursor solution was prepared by sequentially dissolving 2.0 g $Co(NO_3)_2{\cdot}6H_2O$, 0.6 g thiourea, and 0.8 g PVP in 70 mL ethylene glycol under vigorous magnetic stirring for 30 min. The homogeneous mixture was hydrothermally treated in a Teflon-lined autoclave at 140 °C for 24 h. After cooling, the resultant product was collected via centrifugal washing with acetone, deionized water, and ethanol. The white powder obtained after drying at 70 °C was ZnS NPs.

ZIF-67: Separate methanolic solutions containing 0.001 $mol{\cdot}L^{-1}$ $Co(NO_3)_2{\cdot}6H_2O$ and 0.004 $mol{\cdot}L^{-1}$ 2-MIM were prepared. The $Co(NO_3)_2$ solution was titrated dropwise into the 2-MIM solution under continuous stirring. After aging at 25 °C for 6 h, the purple ZIF-67 crystals were isolated through centrifugation with methanol, followed by vacuum drying at 60 °C.

Co/NC: ZIF-67 powder was pyrolyzed in a tube furnace under N_2 atmosphere with a heating ramp of 5 °C·min^{-1} to 800 °C and a dwell time of 3 h. The resulting black carbonaceous material was designated as Co/NC.

Co@ZCS/NSC: A 1:10 mass ratio of ZnS and ZIF-67 powder was physically homogenized. The mixture was calcined under identical pyrolysis conditions to Co/NC (800 °C/3 h/N_2), yielding the Co@ZCS/NSC.

Co/NSC: The Co@ZCS/NSC composite was stirred in 3 mol·L^{-1} HNO_3 for 6 h to remove metallic nanoparticles. After washed with deionized water, the acid-treated sample (noted as Co/NSC) was recovered by vacuum filtration and dried at 60 °C;

1.3. Physical characterization.

The crystalline structure and phase composition of the catalysts were investigated using X-ray diffraction (XRD, Rigaku SmartLab, Cu Kα radiation) and Raman spectroscopy (Horiba LabRAM HR-800, 633 nm). Morphological evaluations were conducted through cold-field emission scanning electron microscopy (SEM, Hitachi SU8600 at 5 kV), and high-resolution transmission electron microscopy (HR-TEM, FEI Tecnai-G2 F20 operated at 200 kV) coupled with selected-area electron diffraction (SAED), high-angle annular dark-field-scanning TEM (HAADF-STEM) capabilities, and energy-dispersive X-ray spectroscopy (EDS). Surface chemical states were analyzed by X-ray photoelectron spectroscopy (XPS, Thermo Fisher ESCALAB 250Xi, Al Kα), with binding energies calibrated against the C 1s peak at 284.8 eV.

Nitrogen physisorption measurements (Micromeritics ASAP 2020 M system) were performed on determine specific surface areas via the Brunauer-Emmett-Teller (BET) method and pore size distributions using the Barrett-Joyner-Halenda (BJH) model.

1.4. Electrochemical measurements.

The ORR and OER performances were evaluated using a three-electrode configuration with a rotating ring-disk electrode system (RRDE-3A, ALS Co., Ltd., Japan) interfaced with a CHI 760E electrochemical workstation (China). All measurements were performed in O_2-saturated 0.1 mol·L^{-1} KOH electrolyte maintained at room temperature. The three-electrode system comprised a glassy carbon working electrode, a graphite rod counter electrode, and a Hg/HgO reference electrode, with the catalyst uniformly loaded at 0.4 mg·cm^{-2} via drop-casting methodology. Catalyst inks were prepared by ultrasonically dispersing 5 mg catalyst in 900 μL ethanol and 25 μL Nafion solution. Cyclic voltammetry (CV) and linear sweep voltammetry (LSV) measurements were conducted at 50 mV·s^{-1} and 5 mV·s^{-1}, respectively. Electrochemical impedance spectroscopy (EIS) was performed at the $E_{1/2}$ potential of ORR across a frequency range of 10^6~0.01 Hz. Catalyst durability was quantified via accelerated degradation testing (ADT) and chronoamperometric (CA) measurements. All potentials were converted to the reversible hydrogen electrode (RHE) scale using E (vs. RHE) = E (vs. Hg/HgO) + 0.059*pH + 0.198. The Tafel slope is also determined from the K-L equation. The electron transfer number (n) for the ORR was determined by calculating the linear slope of J^{-1} versus $\omega^{-1/2}$ plots, according to the Koutecký–

Levich (K-L) equation. Besides, the H_2O_2 yield (%) and *n* were calculated based on Rotating Ring Disc Electrode (RRDE) datas. Double-layer capacitance (C_{dl}) was calculated from cyclic voltammetry (CV) scans at 20–100 mV·s^{-1} in the non-Faradaic region (1.02–1.1V vs. RHE). ECSA = C_{dl}/C_s, with C_s denoting specific capacitance (0.05 mF·cm^{-2} for 0.1 M KOH).

1.5. Assembly and test of ZABs.

A ZAB was constructed utilizing a zinc plate anode and a Co@ZCS/NSC-catalyzed air cathode, with the electrolyte consisting of 6 mol·L^{-1} KOH and 0.2 mol·L^{-1} $Zn(CH_3COO)_2$. The catalyst ink was formulated by homogeneously dispersing 1 mg catalyst, 1 mg acetylene black, and 10 μL Nafion solution in 260 μL ethanol, followed by ultrasonic agitation for 30 min. This ink was uniformly coated onto carbon paper, resulting in a catalyst loading of 1 mg·cm^{-2}. Comparative electrodes employing commercial Pt/C and a Pt/C||RuO_2 mixture (1:1 mass ratio) were fabricated under identical loading conditions to enable performance benchmarking.

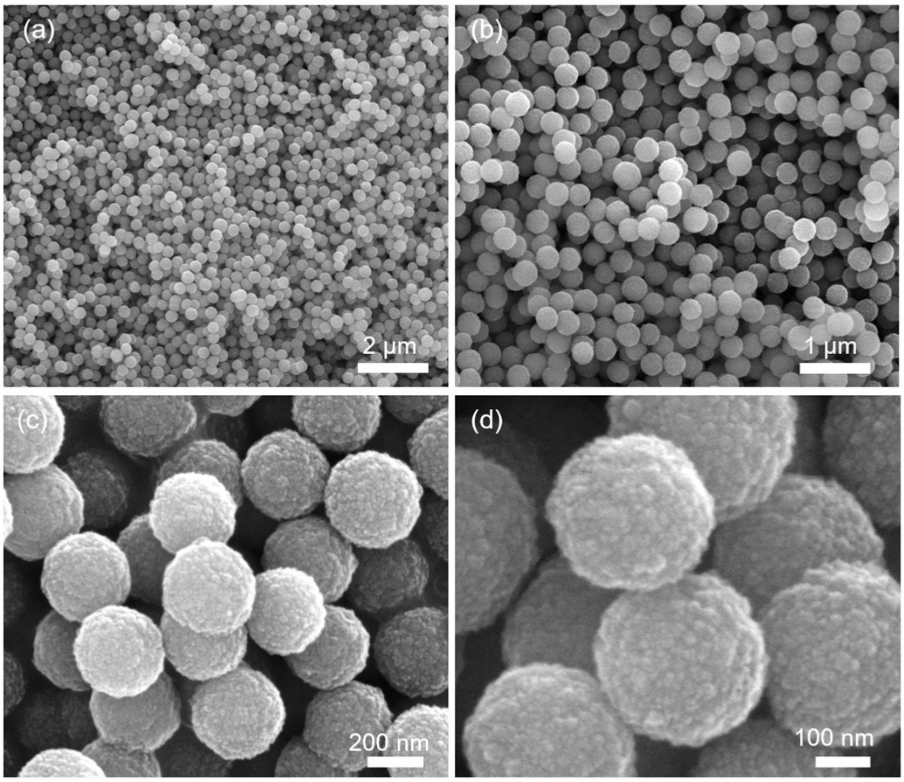

Figure S1. SEM images of ZnS nanospheres.

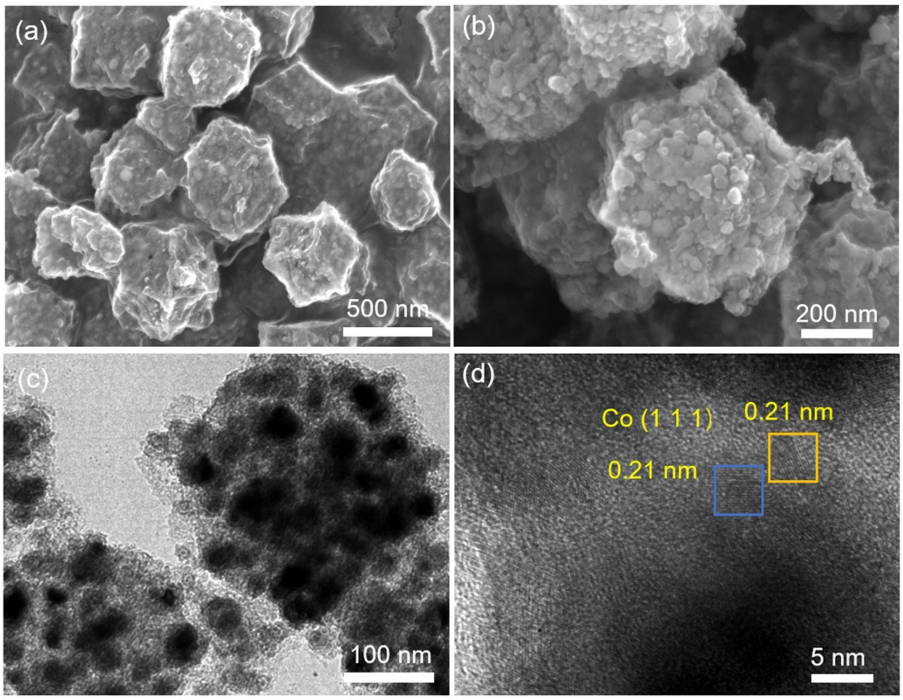

Figure S2. (a,b) SEM and (c,d) TEM images of Co/NC.

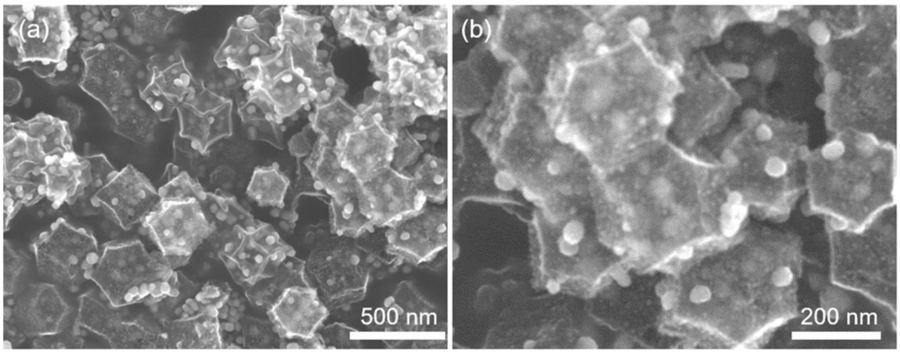

Figure S3. SEM images of Co@ZCS/NSC.

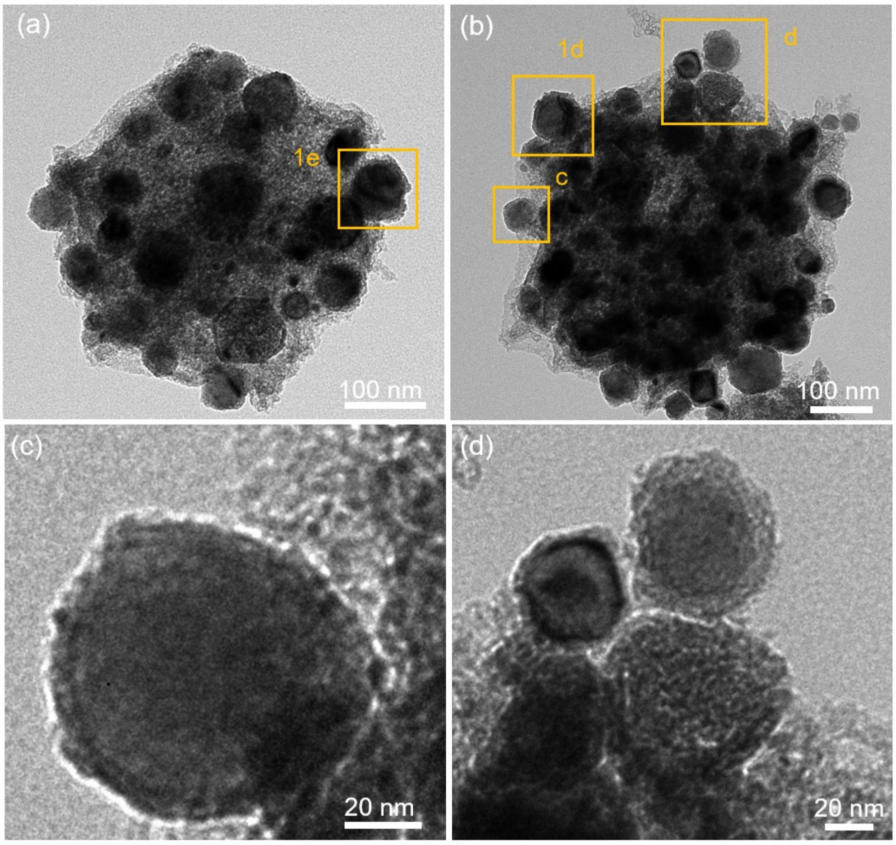

Figure S4. TEM images of Co@ZCS/NSC.

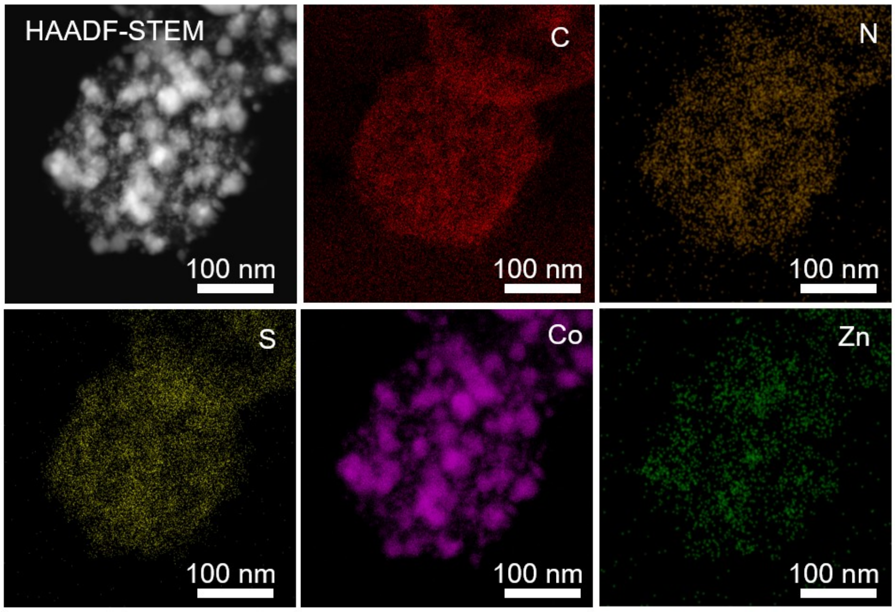

Figure S5. HAADF-STEM and EDS elemental mapping images of Co@ZCS/NSC.

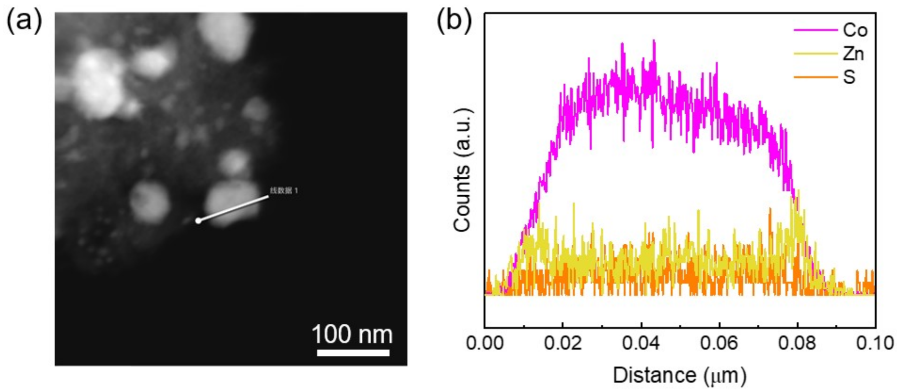

Figure S6. (a) STEM-EDS and (b) line-scan curves of Co@ZCS/NSC.

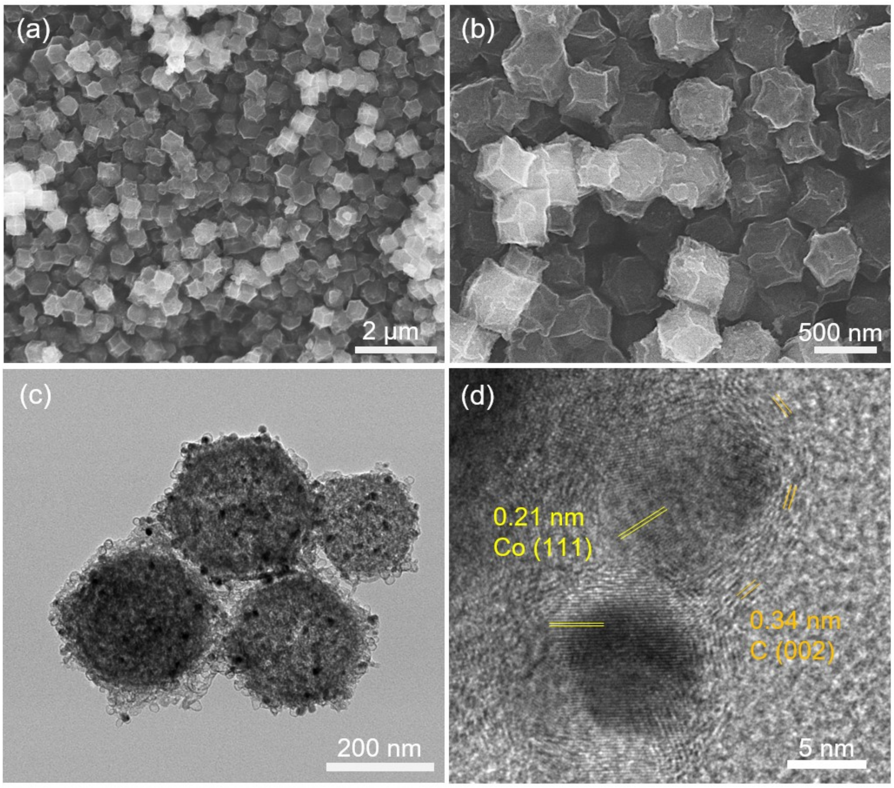

Figure S7. (a,b) SEM and (c,d) TEM images of Co/NSC.

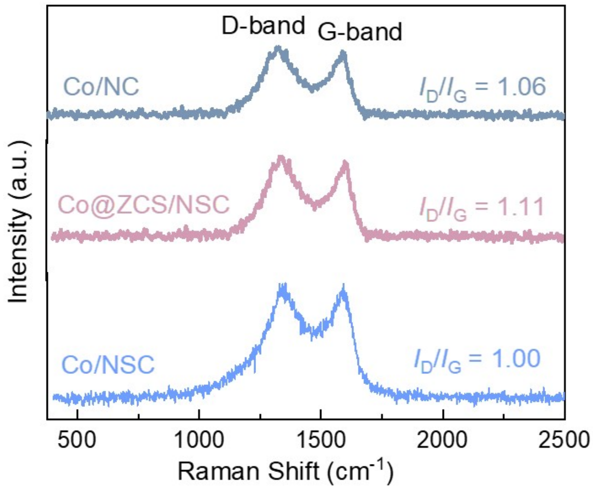

Figure S8. Raman spectra of samples.

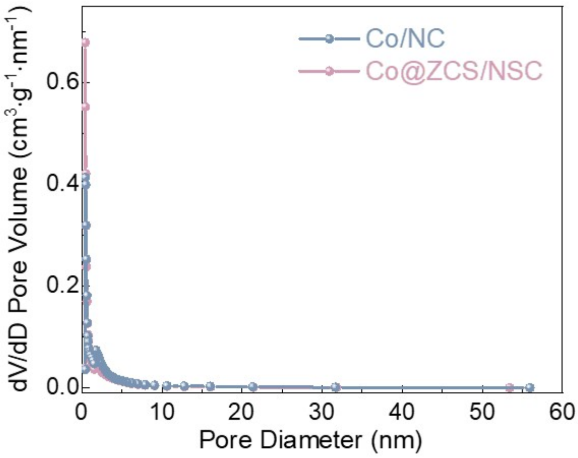

Figure S9. Pore size distribution of samples.

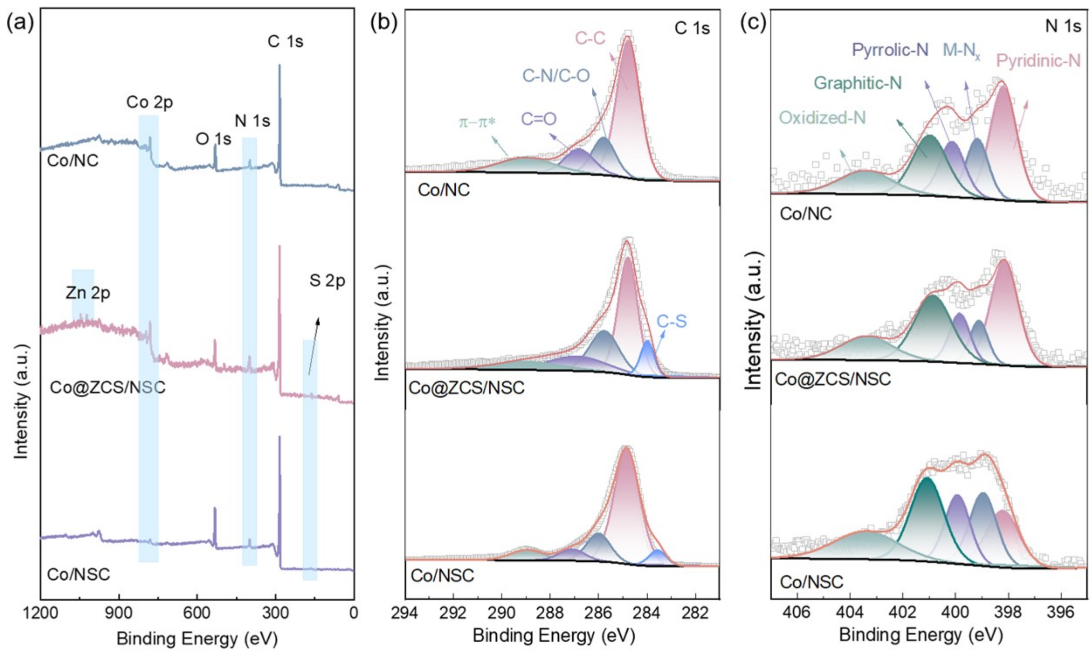

Figure S10. (a) XPS survey spectra, high-resolution XPS spectra of (b) C 1s and (c) N 1s of samples.

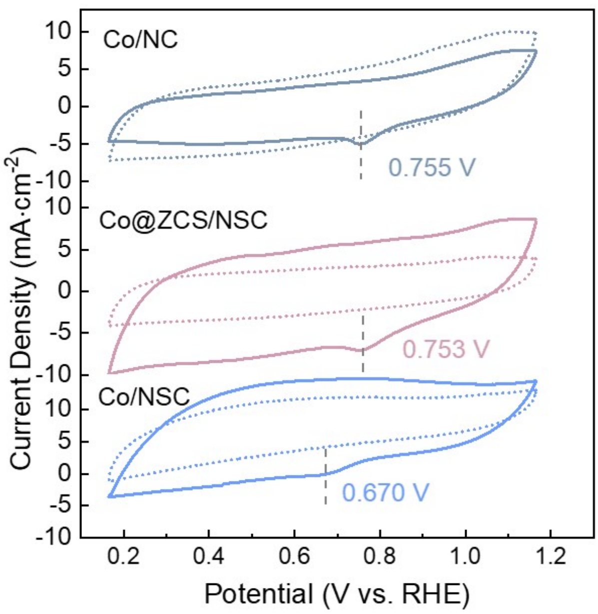

Figure S11. CV curves under O_2 (solid lines) and N_2 (dotted lines) atmosphere in 0.1 mol L^{-1} KOH of samples.

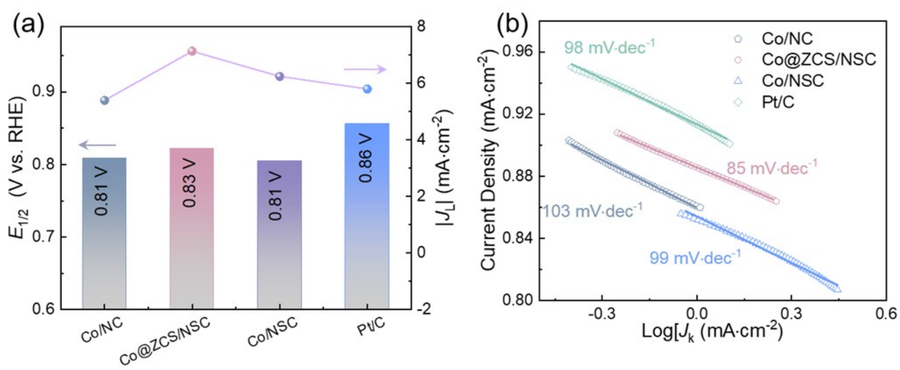

Figure S12. (a) $E_{1/2}$ and $|J_L|$ and (b) Tafel slopes for ORR of as-prepared samples.

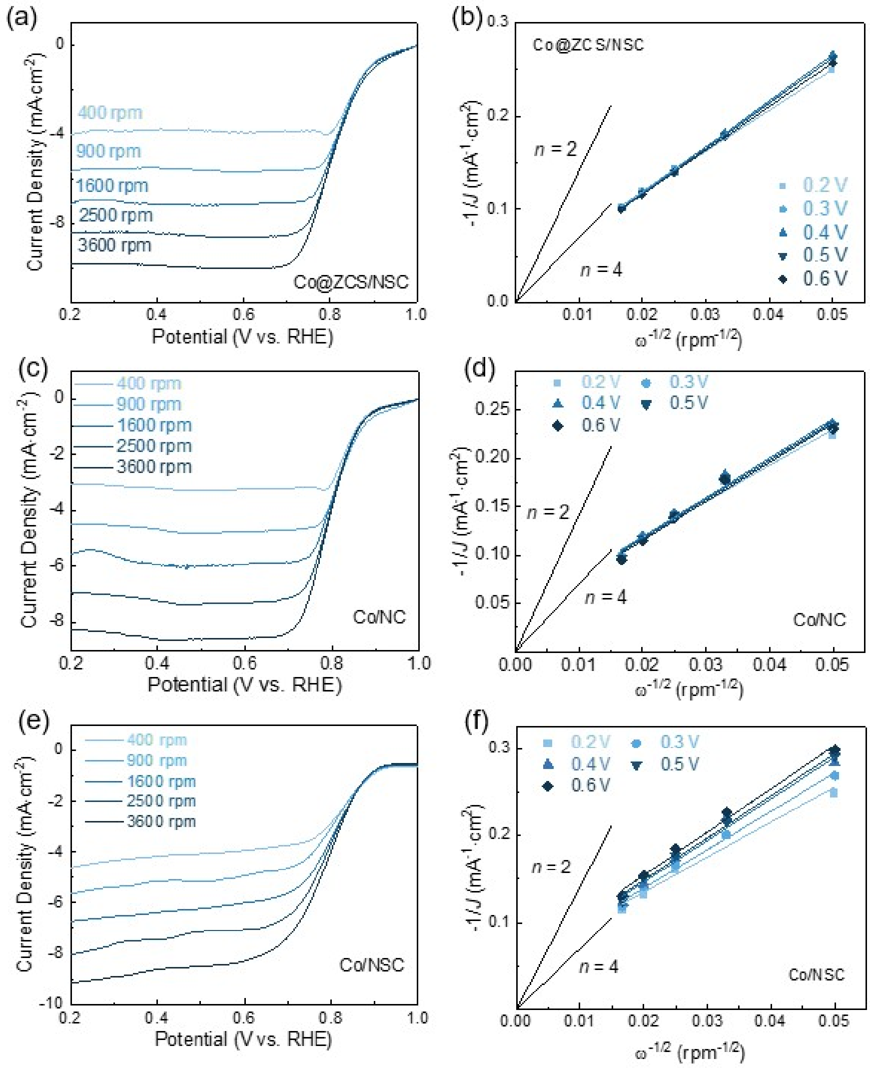

Figure S13. LSV curves with different scan speeds and corresponding K-L plots of samples.

=

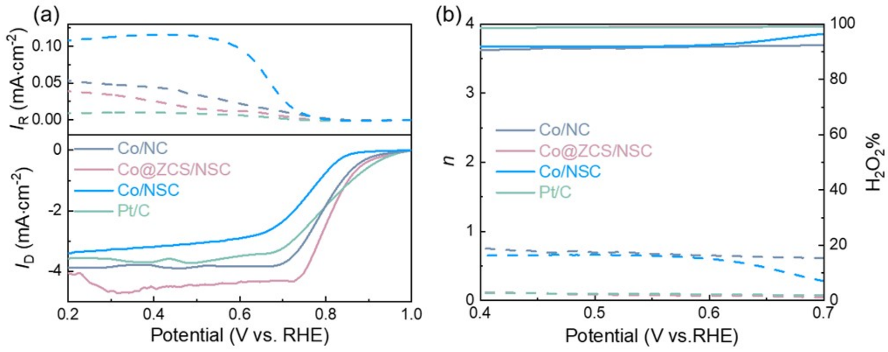

Figure S14. (a) Disk (I_D) and ring (I_R) current density of ORR obtained with LSVs on RRDE for samples with different temperatures; (b) Calculated electron transfer number (n) and peroxide yield (% H_2O_2) based on the corresponding RRDE data.

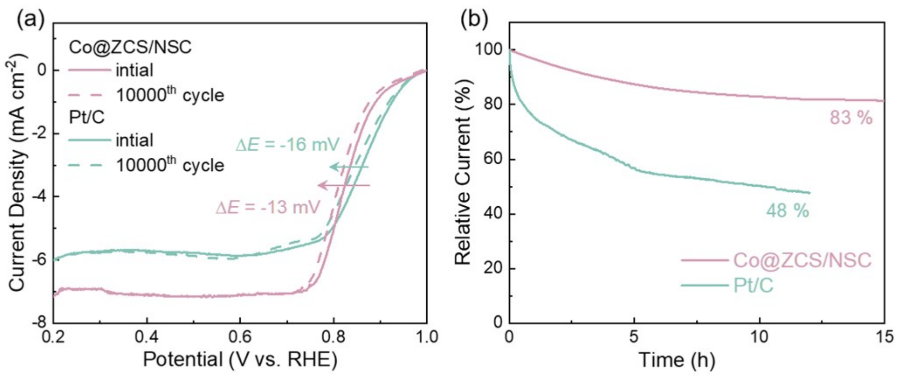

Figure S15. ORR stability based on chronoamperometric measurements of samples.

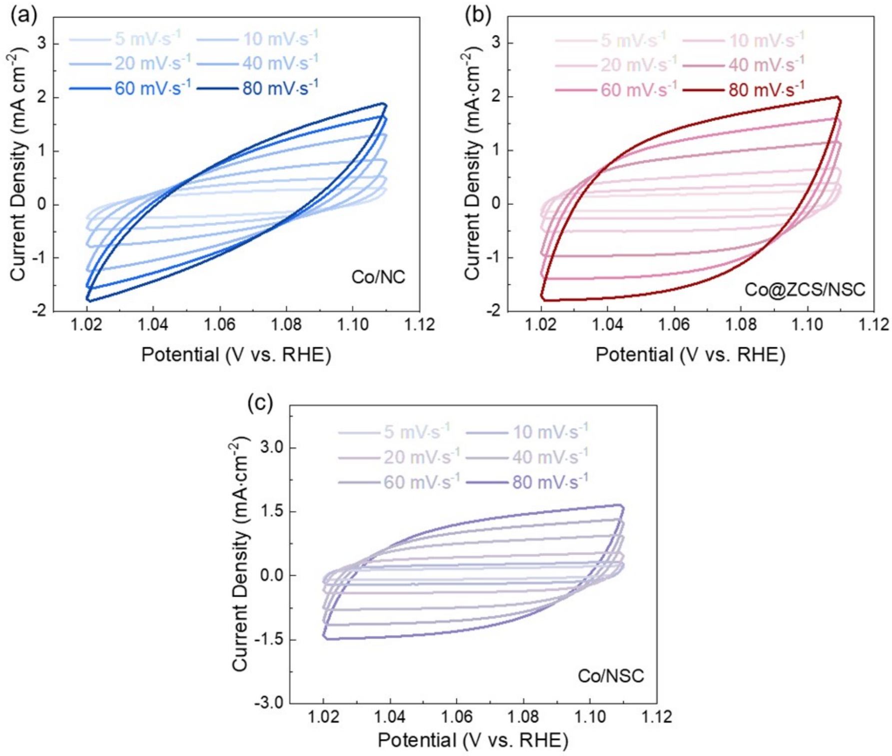

Figure S16. CV curves at varied rates within the non-faradaic region of samples.

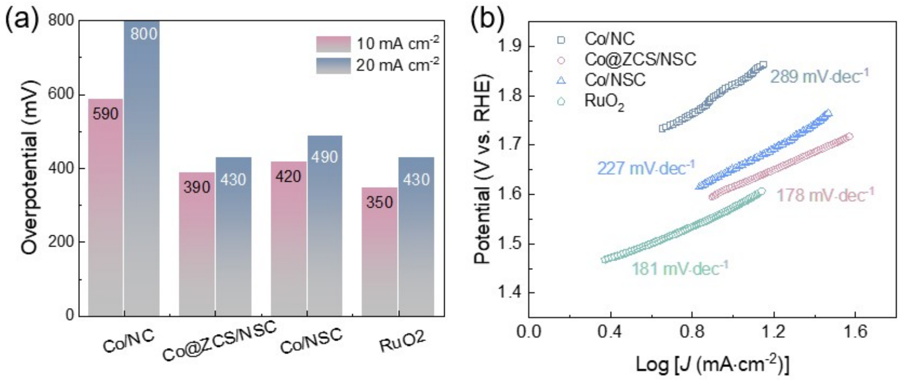

Figure S17. (a) Overpotentials at 10/20 mA·cm⁻² and (b) Tafel slopes for OER of as-prepared samples.

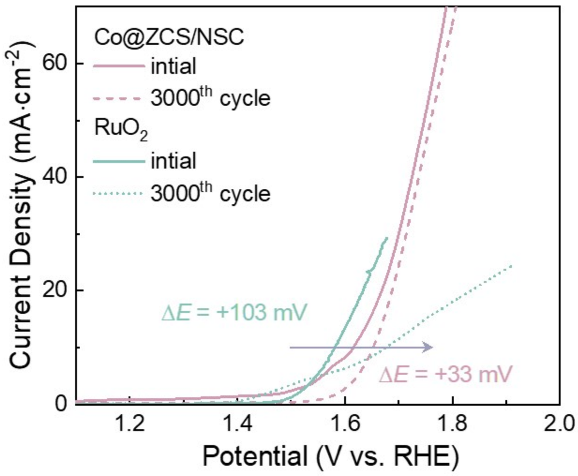

Figure S18. Cycling stability for OER of samples.

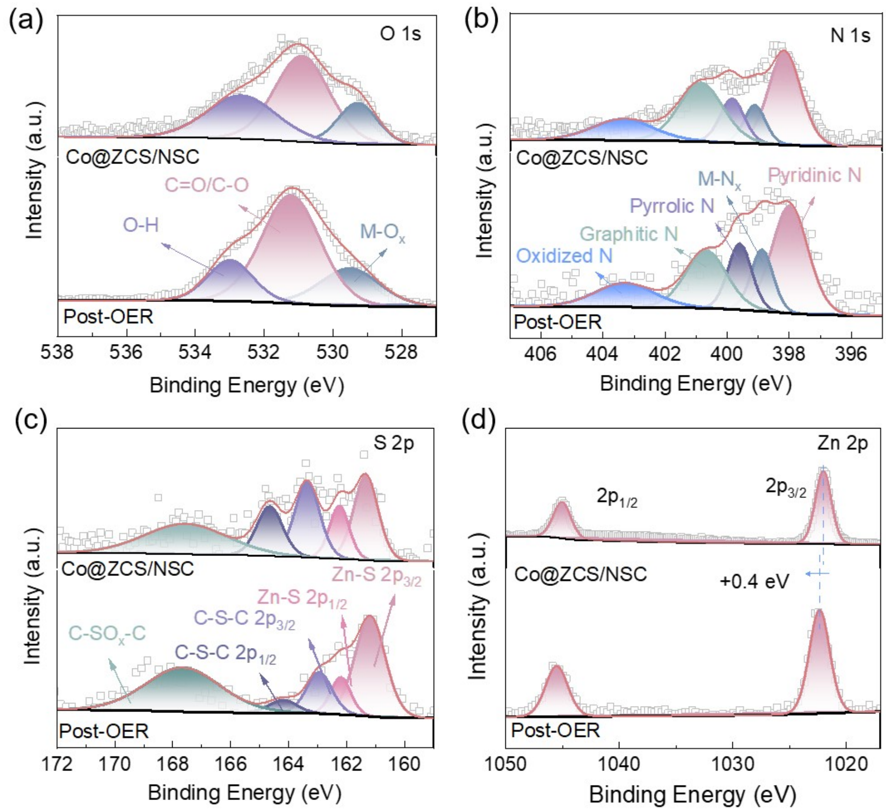

Figure S19. High-resolution XPS spectra of samples before and after OER corresponding to (a) O 1s, (b) N 1s, (c) S 2p, and (d) Zn 2p.

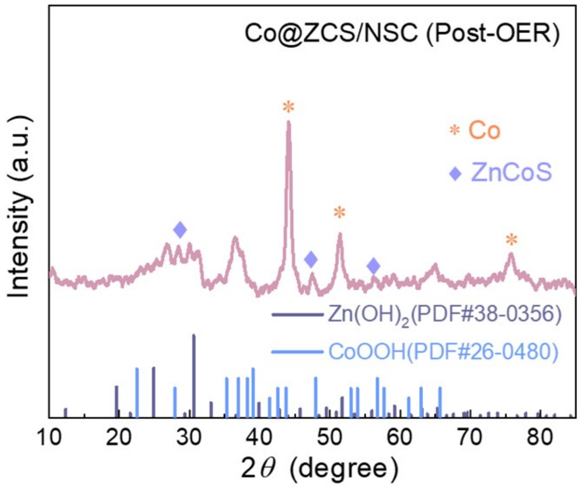

Figure S20. XRD pattern of Co@ZCS/NSC after OER.

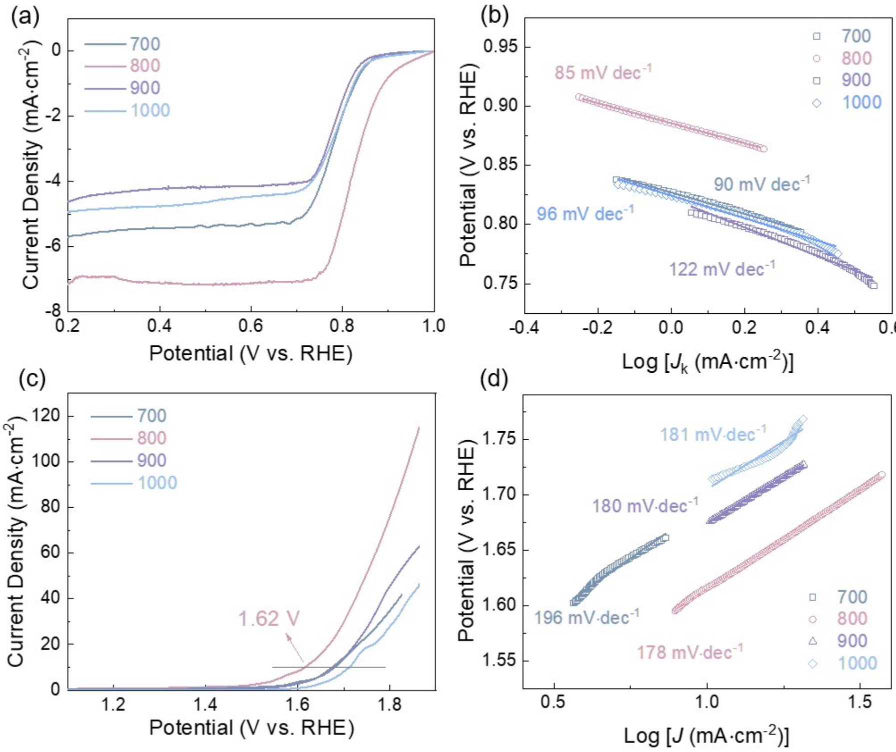

Figure S21. LSV curves and Tafel slopes for (a,b) ORR and (c,d) OER of Co@ZCS/NSC with varying pyrolysis temperatures.

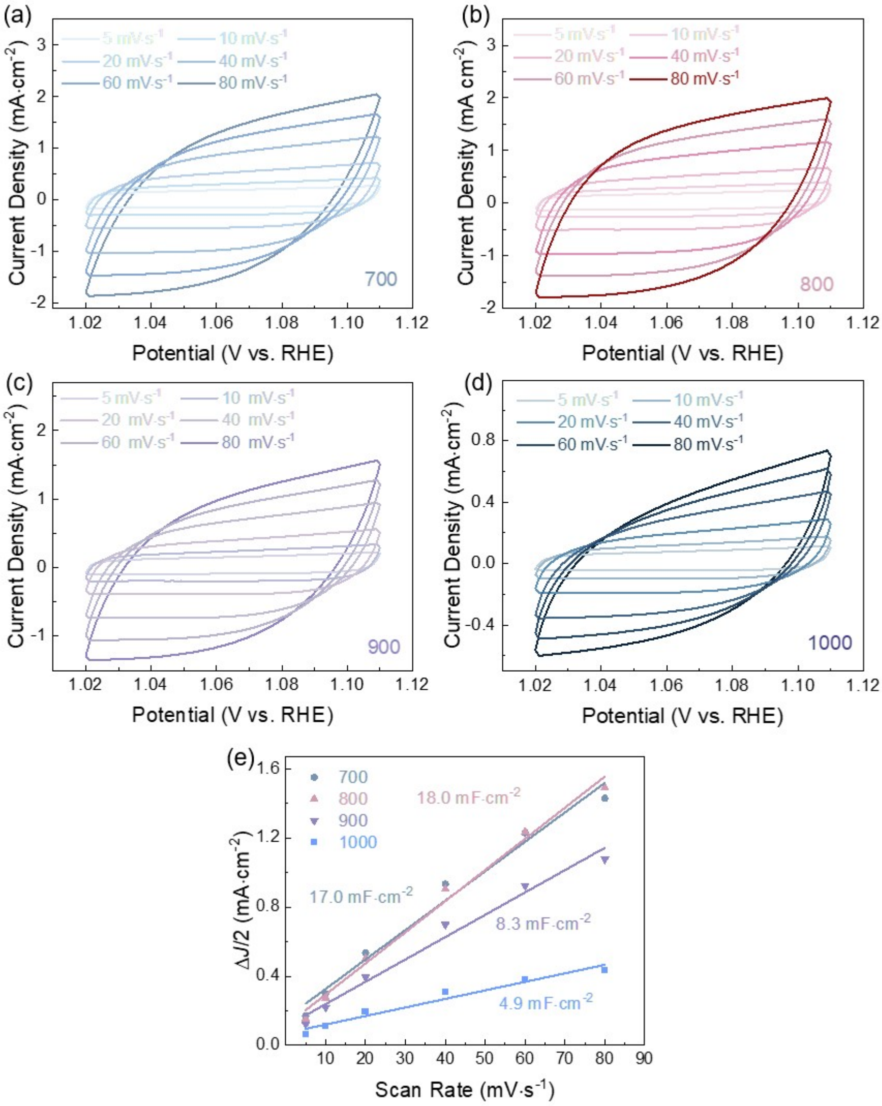

Figure S22. (a-d) CV curves at varied rates within the non-faradaic region and linear fitting of (e) C_{dl} of Co@ZCS/NSC with varying pyrolysis temperatures.

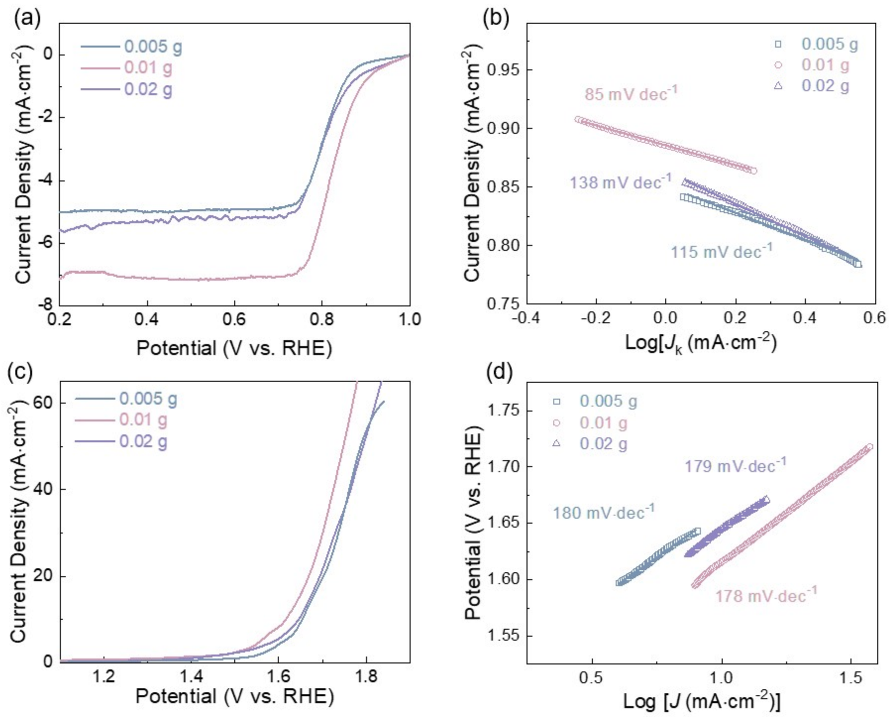

Figure S23. LSV curves and Tafel slopes for (a,b) ORR and (c,d) OER of Co@ZCS/NSC with different mass of ZnS nanospheres.

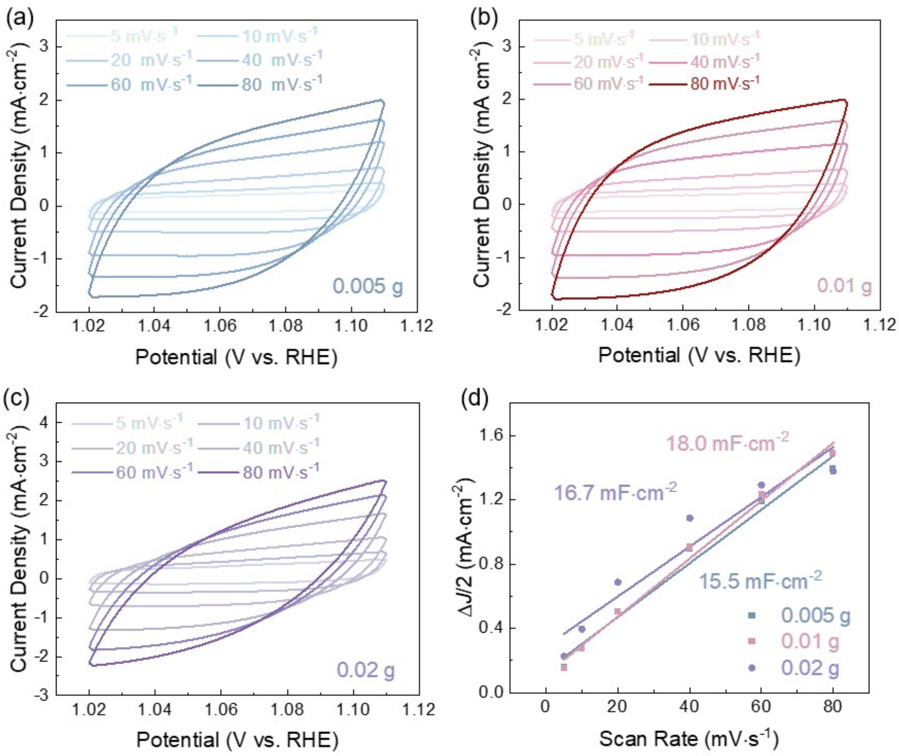

Figure S24. (a-c) CV curves at varied rates within the non-faradaic region and linear fitting of (d) C_{dl} of Co@ZCS/NSC with different mass of ZnS nanospheres.

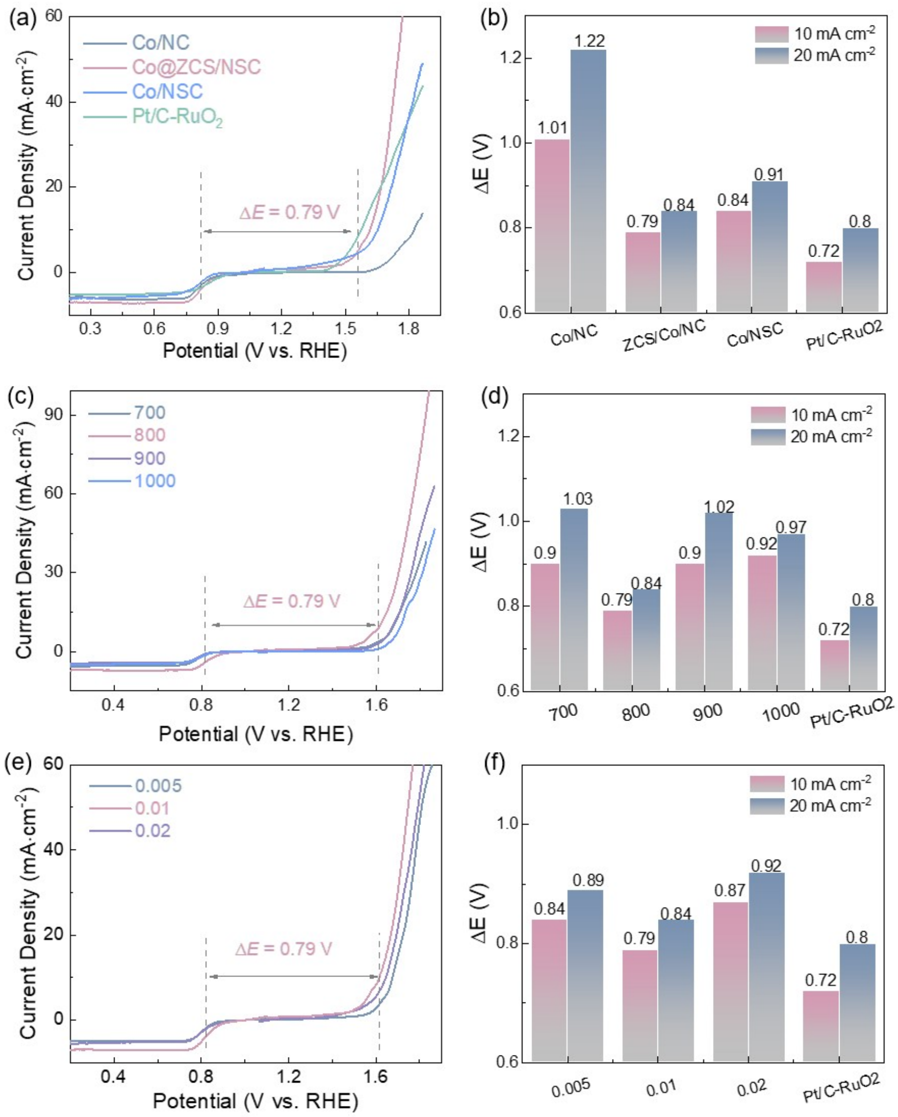

Figure S25. The potential gap between ORR and OER of different sample series.

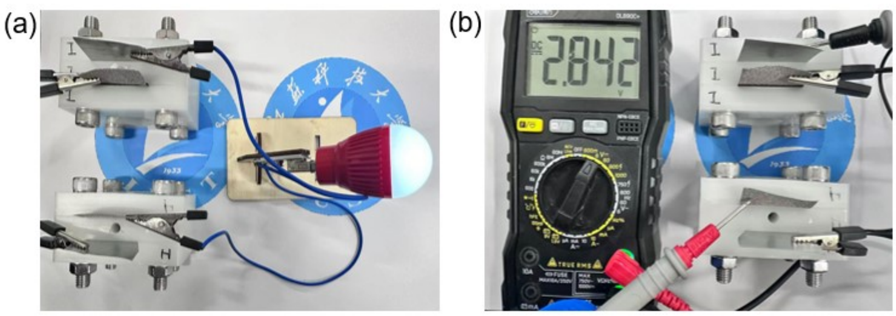

Figure S26. (a) Small bulb powered by two serially connected Co@ZCS/NSC-catalyzed ZABs and (b) post-operation OCV.

Table S1. BET surface area, pore volume, mesoporous and microporous diameter of samples

Catalyst	BET surface area (m^2/g)	pore volume (cm^3/g)	mesoporous diameter (nm)	microporous diameter (nm)
Co/NC	344	0.29	4.93	0.56
Co@ZCS/NSC	347	0.26	6.09	0.52

Table S2. Relative atomic content of samples determined by XPS analysis.

Catalyst	C at%	N at%	O at%	Co at%	S at%	Zn at%
Co/NC	90.1	3.2	6.2	2.9	-	-
Co@ZCS/NSC	81.8	4.1	8.4	2.4	1.9	1.4
Co/NSC	80.9	5.4	12.2	0.6	0.9	-

Table S3. Calculated *n* and H_2O_2% based on RRDE data of samples with different temperature.

Catalysts	Transfer electron number (n)	Peroxide yield (H_2O_2%)
Co/NC	3.6~3.7	15~20
Co@ZCS/NSC	3.9~4.0	1~5
Co/NSC	3.6~3.9	7~16
Pt/C	3.9~4.0	1~5

Table S4. Fitting results of EIS for the samples.

	Rs (Ω)	Err%	Rc (Ω)	Err%	Rct (Ω)	Err%
Co@ZCS/NSC	48	0.5	33	5.2	41	5.8
Co/NC	50	0.3	58	29.3	120	6.2
Co/NSC	51	1.2	46	29.4	277	4.7
ZnS	51	1.8	380	12.3	1220	6.6

Table S5. Relative atomic content of Co@ZCS/NSC before and after OER determined by XPS analysis.

Catalyst	C at%	N at%	O at%	Co at%	S at%	Zn at%
Co@ZCS/NSC	81.8	4.1	8.4	2.4	1.9	1.4
Co@ZCS/NSC After OER	70.9	4.7	19.1	2.2	1.7	1.4

Table S6. Comparison of ORR and OER performance with those reported relative bifunctional electrocatalysts.

Catalyst	ORR $\|J_L\|$ (mA cm^{-2})	ORR $E_{1/2}$ (V vs. RHE)	OER Overpotential @10 mA cm^{-2} (mV)	Reference
Co@ZCS/NSC	7.2	0.83	390	This work
Pt/C‖RuO_2	5.2	0.86	350	This work
ZnS@C-2	5.0	0.82	377	S1
ZnS/NSC-1000	5.4	0.86	-	S2
ZnS@NC-3	5.0	0.84 V	-	S3
Co-ZIF/CNF	3.7	0.85 V	390	S4
NiCoOS	6.0	0.79	470	S5
ZIF-67–6	5.24	0.83 V	270 (1 M KOH)	S6
Co/NMHCS	5.9	0.83	335 (1 M KOH)	S7
FeCo-1/NSC	6.6	0.82	325 (1 M KOH)	S8
Co/N–C-800	5.6	0.82	274 (1 M KOH)	S9
Co/CNT/MCP-850	4.8	0.80	270 (1 M KOH)	S10
FeS_2-CoS_2/NCFs	5.6	0.81	340	S11
Co_4N@NC-m	5.2	0.87	398	S12
CoO-Mn_3O_4	7.1	0.77	-	S13
CoO/C	4.5	0.78	-	S14
Co_2P-40/VC	5.0	0.77	-	S15
Fe-NC SAC	-	0.88	450	S16

Pt-SCFP/C-12	-	0.81	370	S17
N-Co_3O_4@NC	-	0.77	266 (1 M KOH)	S18
Co_3HITP_2	-	0.80	-	S19
P-doped-Co@NC	-	-	340	S20
NC@Co-1000	-	-	380	S21
sf_4-CoS_x	-	-	375	S22

References

[S1] Lin, C., Yin, Y., Wang, G., Cao, X., Ma, J. Carbon-coated ZnS as a high-performance ORR/OER bifunctional cathode catalyst for zinc-air batteries. *International Journal of Hydrogen Energy*, *93*, (2024) 221-228.

[S2] Peng, Y., Zhang, F., Zhang, Y., Luo, X., Chen, L., Shi, Y. ZnS modified N, S dual-doped interconnected porous carbon derived from dye sludge waste as high-efficient ORR/OER catalyst for rechargeable zinc-air battery. *Journal of Colloid and Interface Science*, *616*, (2022) 659-667.

[S3] Li, Y., Wang, C., Cui, M., Chen, S., Gao, L., Liu, A., Ma, T. Facile synthesis of ZnS decorated N, S co-doped carbon polyhedron as high efficiency oxygen reduction reaction catalyst for Zn-air battery. *Applied Surface Science*, *509*, (2020) 145367.

[S4] He, H., Lei, Y., Liu, S., Thummavichai, K., Zhu, Y., Wang, N. Tunable active-sites of Co–nanoparticles encapsulated in carbon nanofiber as high performance bifunctional OER/ORR electrocatalyst. *Journal of colloid and interface science*, *630*, (2023) 140-149.

[S5] Bai, Z., Li, S., Fu, J., Zhang, Q., Chang, F., Yang, L., Lu J., Chen, Z. Metal-organic framework-derived Nickel Cobalt oxysulfide nanocages as trifunctional electrocatalysts for high efficiency power to hydrogen. *Nano Energy*, *58*, (2019) 680-686.

[S6] Ju, Y., Huang, W., Gao, Z., Liu, M., Huang, N. Research on ORR and OER performance of Co based catalyst from ZIF-67. *Applied Materials Today*, *42*, (2025). 102576.

[S7] Diao, J., Wang, S., Yang, Z., Qiu, Y., Xu, R., Wang, W., Chen, K., Li, X., Chao, T., Guo, X., Qu, Y. Interfacial electron distribution of Co nanoparticles supported on N-doped mesoporous hollow carbon spheres endows highly efficient ORR, OER, and HER. *Advanced Materials Interfaces, 10*(14), (2023) 2202394.

[S8] Chang, S., Zhang, H., Zhang, Z. FeCo alloy/N, S dual-doped carbon composite as a high-performance bifunctional catalyst in an advanced rechargeable zinc-air battery. *Journal of Energy Chemistry*, *56*, (2021) 64-71.

[S9] Fan, X. Z., Du, X., Pang, Q. Q., Zhang, S., Liu, Z. Y., Yue, X. Z. In situ

construction of bifunctional N-doped carbon-anchored Co nanoparticles for OER and ORR. *ACS Applied Materials & Interfaces*, *14*(6), (2022) 8549-8556.
[S10] Zhou, X., Liu, X., Zhang, J., Zhang, C., Yoo, S. J., Kim, J. G., Chu, X., Song, C., Wang, P., Zhao, Z., Li, D., Zhang, W., Zheng, W. Highly-dispersed cobalt clusters decorated onto nitrogen-doped carbon nanotubes as multifunctional electrocatalysts for OER, HER and ORR. *Carbon*, *166*, (2020) 284-290.
[S11] Shi, X., He, B., Zhao, L., Gong, Y., Wang, R., & Wang, H. FeS_2–CoS_2 incorporated into nitrogen-doped carbon nanofibers to boost oxygen electrocatalysis for durable rechargeable Zn-air batteries. *Journal of Power Sources*, *482*, (2021) 228955.
[S12] Chen, L., Zhang, Y., Liu, X., Long, L., Wang, S., Xu, X., Liu, M., Yang, W., Jia, J. Bifunctional oxygen electrodes of homogeneous Co_4N nanocrystals@N-doped carbon hybrids for rechargeable Zn-air batteries. *Carbon*, *151*, (2019) 10-17.
[S13] Choi, J. H., Chun, H., Kim, D. W., Kabiraz, M. K., Kim, J., Kim, J., Kim, K. H., Wang, B., Jeong, H. M., Choi, S. I., Kang, J. K. Zeolitic imidazolate framework-derived bifunctional CoO-Mn_3O_4 heterostructure cathode enhancing oxygen reduction/evolution via dynamic O-vacancy formation and healing for high-performance Zn-air batteries. *Energy Storage Materials*, *75*, (2025) 104040.
[S14] Liu, J., Bao, H., Zhang, B., Hua, Q., Shang, M., Wang, J., Jiang, L. Geometric occupancy and oxidation state requirements of cations in cobalt oxides for oxygen reduction reaction. *ACS applied materials & interfaces, 11*(13), (2019) 12525-12534.
[S15] Parra-Puerto, A., Ng, K. L., Fahy, K., Goode, A. E., Ryan, M. P., Kucernak, A. Supported transition metal phosphides: activity survey for HER, ORR, OER, and corrosion resistance in acid and alkaline electrolytes. *ACS Catalysis*, *9*(12), (2019) 11515-11529.
[S16] Du, C., Gao, Y., Wang, J., Chen, W. A new strategy for engineering a hierarchical porous carbon-anchored Fe single-atom electrocatalyst and the insights into its bifunctional catalysis for flexible rechargeable Zn–air batteries. *Journal of Materials Chemistry A*, *8*(19), (2020) 9981-9990.
[S17] Wang, X., Sunarso, J., Lu, Q., Zhou, Z., Dai, J., Guan, D., Zhou, W., Shao, Z.

High-performance platinum-perovskite composite bifunctional oxygen electrocatalyst for rechargeable Zn–air battery. *Advanced Energy Materials*, *10*(5), (2020) 1903271.

[S18] Wang, Z., Xu, W., Chen, X., Peng, Y., Song, Y., Lv, C., Liu, H., Sun, J., Yuan, D., Li, X., Guo, X., Yang, D., Zhang, L. Defect-rich nitrogen doped Co_3O_4/C porous nanocubes enable high-efficiency bifunctional oxygen electrocatalysis. *Advanced Functional Materials, 29*(33), (2019) 1902875.

[S19] Lian, Y., Yang, W., Zhang, C., Sun, H., Deng, Z., Xu, W., Song, L., Ouyang, Z., Wang, Z., Guo, J., Peng, Y. Unpaired 3d electrons on atomically dispersed cobalt centres in coordination polymers regulate both oxygen reduction reaction (ORR) activity and selectivity for use in zinc–air batteries. *Angewandte Chemie International Edition*, *59*(1) (2020) 286-294.

[S20] Li, Y., Jia, B., Fan, Y., Zhu, K., Li, G., Su, C. Y. Bimetallic zeolitic imidazolite framework derived carbon nanotubes embedded with Co nanoparticles for efficient bifunctional oxygen electrocatalyst. *Advanced Energy Materials*, 8(9), (2018) 1702048.

[S21] Pereira, G. M., Cellet, T. S., Gonçalves, R. H., Rubira, A. F., Silva, R. Trapped metallic cobalt nanoparticles in doped porous graphite: An electrocatalyst that gets better over reaction time. *Applied Catalysis B: Environmental*, *217*, (2017) 144-153.

[S22] Kim, M. S., Naveen, M. H., Khan, R., Bang, J. H. Iterative oxidation and sulfidation reactions: revival of bulk cobalt sulfide into an active electrocatalyst for the oxygen evolution reaction. *Journal of Materials Chemistry A*, *8*(16), (2020) 7647-7652.